Analytical modelling of the influence of local mixed mode displacements on roughness induced crack closure

N. Kamp[a,b], N. Gao[a], M.J. Starink[a], M.R. Parry[c], I. Sinclair[a,*]

[a] Materials Research Group, School of Engineering Sciences, University of Southampton,UK

[b] Currently at School of Materials, University of Manchester, UK

[c] Damage Tolerance Department (ESADU), Airbus, Filton, Bristol, UK

[*] Corresponding author. Materials Research Group, University of Southampton, Highfield, Southampton, SO17 1BJ, UK. Tel.: +44-(0)2380595095; Fax: +44-(0)2380593016; *E-mail address*: I.Sinclair@soton.ac.uk (I. Sinclair)

Keywords: Fatigue crack growth, roughness induced crack closure, modelling, 2xxx aluminium alloys.

Abstract

Application of crack closure analytical modelling to predict the behaviour of complex fatigue crack growth properties is limited partly due to restricted two dimensional modelling approaches. An analytical model of roughness induced crack closure (RICC) is developed in the present paper considering a three dimensional twisted and kinked crack path. Residual shear deformations at asperities in the crack wake affect the crack opening generating closure. These residual shear deformations are explicitly formulated from

residual plastic deformation. The respective influence of the in-plane and out-of-plane deformation on RICC is discussed. The crack twisting is found to be a less significant effect on the RICC than the crack kinking, for similar deviation angles. However, these out-of-plane crack deflections are found to be non negligible particularly at low tilting angles. This analytical model is used to predict the closure stress intensity factor for a range of 2xxx aluminium alloys. Predictions are compared to experimental results obtained from low ΔK fatigue crack growth tests. Experimental results show that fatigue performance scale with closure level and roughness of the failed fatigue specimen surfaces. Comparison of estimated and measured closure stress intensity factor show similar trends.

1 Introduction

Fatigue crack growth performance is a key parameter in the design of aerospace engineering structures. Fatigue crack growth in aluminium alloys is widely thought to be influenced by crack shielding processes such as crack closure (see e.g. [1,2]). Various studies have reported that the fatigue crack growth behaviour of aluminium alloys is affected by roughness induced crack closure (RICC), particularly near threshold [3,4]. Attempts have therefore been made to model analytically or through FE analysis the influence of RICC on fatigue crack growth performance [5,6]. However, both analytical and FE model are limited in their application to real materials by their two dimensional simplified geometries as opposed to the three dimensional, irregular nature of real crack paths. The significance of three dimensional crack shapes has been highlighted in recent studies of the crack closure phenomenon using X-ray computed tomography on 2xxx-

type aluminium alloys [7,8]. Toda *et al*. [8] particularly observed that significant crack closure in terms of contact areas may be attributable to mode III, out-of-plane, displacements of nominally mode I cracks, requiring crack twist about the nominal growth direction. As such, a main aim of the present paper is to develop an understanding of the contribution of mode III deformation to the occurrence of RICC. The modelling approach used is based on a novel analytical model of in-plane RICC developed by the authors in an earlier work [9]. This model relied on a quantitative description of the residual shear deformations involved in a deflected crack path and has been shown to reproduce results obtained via elastic-plastic finite element (FE) analysis of simple, regularly deflecting cracks with a high level of accuracy. Comparison is then made between analytical model predictions and experimental data on crack closure behaviour for a range of 2xxx aluminium alloys.

2 RICC modelling and fracture surface analysis

2.1 In-plane modelling of RICC

An analytical model of in-plane RICC has been described previously [9]. The main steps of the model derivation are described below.

The model is based on a simple regular 'zig-zag' crack geometry, defined by a crack deflection angle, θ, and length, L as shown in Fig. 1a. This analytical model considered: (i) a description of the opening behaviour of the final deflected crack section and (ii) a description of the residual deformation of the asperity in the crack wake. As illustrated schematically in Fig. 1b**,** the model considers that crack closure will occur when

$$\delta_c = h_{II} \sin(2\theta) \quad \text{(Eq. 1)}$$

Where h_{II} is the asperity size and δ_c is the crack tip opening displacement (CTOD) at closure. δ_c is derived from the equation of the elastic stress field displacement in plane strain conditions assuming that the tensile opening of the final section of crack (of length L) can be derived from local mode I stress intensity approximations for a vanishingly small crack deflection [9]

$$CTOD = \frac{4\left(1-\nu^2\right)\sqrt{a^{*2}-x^2}}{E\sqrt{\pi a^*}} \cos^3\left(\theta/2\right) K_I \quad \text{(Eq. 2)}$$

where ν is Poisson ratio, E is Young's modulus, K_I is the applied stress intensity factor, a^* is the deflection length (a^* varies between 0 and L) factor. Closure occurs at the deflection point where x=0 and K_I=K_{cl} (K_{cl} is the crack closure stress intensity factor), therefore

$$\delta_c = \frac{4K_{cl}\left(1-\nu^2\right)\sqrt{a^*}}{E\sqrt{\pi}} \cos^3\left(\theta/2\right) \quad \text{(Eq. 3)}$$

h_{II} the asperity size is equated to the residual crack tip shear displacement at the point where the crack turns to form a new asperity tip [9]

$$h_{II} = \frac{\sqrt{3}K_{\mathrm{Im}ax}^{2}\left(1-\nu^{2}\right)\left(\frac{1}{2}+R+\frac{1}{2}R^{2}\right)}{E\sigma_{0}}\left[\sin^{2}(\theta/2)\cos^{4}(\theta/2)\right] \qquad \text{(Eq. 4)}$$

where K_{Imax} is the maximum applied stress intensity factor, R is the stress ratio, σ_0 is the yield strength.

It can be seen from Fig. 1b) that crack closure will occur when $\delta=h_{II}\sin(2\theta)$. Combining Eq. 3 and Eq. 4 and rearranging them to express the closure level, it follows:

$$\frac{K_{I}}{K_{\mathrm{I}\max}} = \frac{K_{cl}}{K_{\mathrm{I}\max}} = \frac{\sqrt{3\pi}K_{\mathrm{I}\max}\left(\frac{1}{2}+R-\frac{1}{2}R^{2}\right)}{4\sigma_{0}\sqrt{a^{*}}}\sin^{2}(\theta/2)\cos(\theta/2) \qquad \text{(Eq. 5)}$$

The model shows a singularity at each turning point, when a^* tends to zero. However, physically, it is legitimate to assume that the crack must propagate some distance ahead of the deformed material at the asperity turning point for that material to effectively move into the crack wake and generate crack closure. As length dimensions of the crack tip deformation field will scale with the plastic zone size, r_p, the distance over which the crack needs to propagate in order for deformation at the asperity tip to act fully in the closure process is expressed as a ratio, λ, of the plastic zone size. FE modelling suggests a reasonable value for λ to be of the order of 0.4 [9]. To represent the transition in shielding in the region $0 \le a^* < \lambda r_p$ we then identify the term h'_{II} to describe the effective component of h_{II} as a function of a^* (normalised by λr_p):

$$h_{II} = h'_{II}\left(\frac{a^*}{\lambda r_p}\right) \qquad \text{(Eq. 6)}$$

Where h'_{II} is the calculated residual shear displacement from Eq. 4.

The model then considers that at the start of a new deflection the closure is still driven by the previous crack deflection and that the new deflection only progressively dominates the closure level as crack extension occurs. A continuous analytical model is thus obtained and can be expressed combining Eq. 5 and 6 as [9]

$$\frac{K_{cl}}{K_{\mathrm{Im}ax}} = \beta \frac{\sqrt{3\pi}K_{\mathrm{Im}ax}\left(\frac{1}{2}+R-\frac{1}{2}R^2\right)}{4\sigma_0}\sin^2(\theta/2)\cos(\theta/2)L(a^*) \qquad \text{(Eq. 7)}$$

with $L(a^*)=\frac{1}{\sqrt{a^*}}$ for $a^*>\lambda r_p$ and $L(a^*)=\frac{\sqrt{a^*}}{\lambda r_p}$ for $a^*<\lambda r_p$

β is a scaling factor which accounts for the variation in the analytical expressions available for determining the CTSD available in the literature [10,11], (analogous to the differences in plastic zone size predicted by Irwin or Dugdale-type approximations for example [12]). As such, β has little physical significance and may be used as a fitting parameter and may be expected to take values between approximately 1 and 4 based on the various CTSD expressions that exist in the literature [13], allowing for inaccuracy in a simple Dugdale calculation of CTSD (microstructural factors influencing slip character might be expected to influence the accuracy of the Dugdale estimate of CTSD, however, such effects are beyond the scope of the current paper).

Typical modelling results for Eq. 7 are presented in Fig. 2.

2.2 Mode III residual shear deformation

Twist on a nominal mode I crack about the growth direction may give rise to mode III (out-of-plane) shear stresses and, hence, residual shear deformations in a similar manner to those described above and in ref. [9] in relation to crack kinking and mode II contributions to crack closure. A trapezoidal geometry has been arbitrarily chosen for the twisted crack path, in the out-of-plane direction, to study mode III deformation as shown in Fig. 3. This geometry is particularly useful as shear deformations arising from the opposite sides of the trapeze do not interact assuming the smallest of the trapezoid parallel side is much larger than the residual shear deformations.

A similar approach to the one used for mode II deformations can be used to account for mode III deformations. First, a Dugdale-type strip yield model under far field mode III is considered to determine the contribution of mode III stress intensities to the crack tip shear displacement (CTSD) at maximum load under plane strain condition

$$CTSD_{\mathrm{III}\max} = \frac{\sqrt{3}(1+\nu)K^2_{\mathrm{III}\max}}{E\sigma_0} \qquad \text{(Eq. 8)}$$

where $K_{\mathrm{III}max}$ is the far field mode III stress intensity factor. Upon unloading a degree of reversed crack tip sliding will occur

$$\Delta CTSD_{\mathrm{III}} = \frac{\sqrt{3}(1+\nu)\Delta K^2_{III}}{2E\sigma_0} \qquad \text{(Eq. 9)}$$

Mode III residual deformation, h_{III}, is expressed as a residual crack tip shear deformation, $CTSD_{IIIres}$, and is given by the difference between Eq. 9 and Eq. 8

$$h_{III}=CTSD_{IIIres} = CTSD_{IIImax} - \Delta CTSD_{III} \quad \text{(Eq. 10)}$$

$$h_{III} = \frac{\sqrt{3}(1+\nu)\left(2K_{\mathrm{III}\max}^{2} - \Delta K_{III}^{2}\right)}{2E\sigma_0} \quad \text{(Eq. 11)}$$

Residual CTSD of a crack under a far field mode III load is correlated to the residual CTSD of a twist deflected crack by replacing K_{IIImax} by k_3, the local mode III stress intensity factor at the tip of a twist deflected crack. k_3 is given by the equation for the local mode III stress intensity factor at the tip of a pupative twist after Faber and Evans [14]

$$k_3 = K_{31}(\Phi)k_1 + K_{32}(\Phi)k_2 \quad \text{(Eq. 12)}$$

with $K_{31}(\Phi) = \cos^4(\theta/2)\left[\sin\Phi\cos\Phi\left(\cos^2(\theta/2) - 2\nu\right)\right]$

and $K_{32}(\Phi) = \sin^2(\theta/2)\cos^2(\theta/2)\left[\sin\Phi\cos\Phi\left(3\cos^2(\theta/2) - 2\nu\right)\right]$

where Φ is the angle of the deflected crack path at the trapezoid base.

and $k_1 = \cos^3(\theta/2)K_I$, $k_2 = \sin(\theta/2)\cos^2(\theta/2)K_I$

Eq. 11 can be re-written as

$$k_3 = g_1(\theta,\Phi)K_I \quad \text{(Eq. 13)}$$

where

$$g_1(\theta,\Phi) = \sin\Phi\cos\Phi\left[\cos^9(\theta/2) - 2\nu\cos^7(\theta/2) + 3\cos^6(\theta/2)\sin^3(\theta/2) - 2\nu\cos^4(\theta/2)\sin^3(\theta/2)\right]$$

It is important to note that these relationships between local stress intensity factors at the tip of a deflected crack and the applied far field stress intensity factor include a notion of sequence of events where the crack is first tilted then twisted, i.e. the projection of the 'tilted' k_1 and k_2 are used to calculate k_3. Obviously no such sequence is expected to occur in a real, complex crack path where shear stresses and deformation in mode II and mode III can freely interact. However, this simplification allows to use well defined non-planar cracks stress intensity factor relationships that are both practical and represent a plausible description of the crack tip stress intensity factors.

Finally, combining Eq. 11 and Eq. 13 gives

$$h_{III} = \frac{\sqrt{3}K_{\mathrm{I}\max}{}^{2}(1+\nu)\left(\frac{1}{2}+R-\frac{1}{2}R^{2}\right)g_1(\theta,\Phi)^2}{E\sigma_0} \qquad \text{(Eq. 14)}$$

2.3 3-Dimensionnal roughness induced crack closure analytical model

Mode III residual deformations associated with a twisted and kinked crack may be incorporated into a similar analytical framework as developed in reference [9] by combining these residual deformations. The schematic drawing of a crack viewed in-plane and out-of-plane in Fig. 4 shows the contribution of mode II and III residual deformation components. Fig. 4 highlights the relationship between the deformations created by the mode II and mode III deformations and the crack opening displacement δ.

Thus crack closure will occur when

$$\delta_c = h \quad \text{with } h = h_{II}\sin(2\theta) + h_{III}\cos\theta\sin\Phi \qquad \text{(Eq. 15)}$$

Therefore combining the equation for h_{III} (Eq. 14) and equations for h_{II} (Eq. 4) and δ_c (Eq. 3) in Eq. 15, the closure level can be expressed as:

$$\frac{K_{cl}}{K_{I\max}} = \beta \frac{\sqrt{3\pi} K_{I\max}\left(\frac{1}{2} + R - \frac{1}{2}R^2\right)}{4\sigma_0} L(a^*)\left[f(\theta) + g_2(\theta,\Phi)\right] \qquad \text{(Eq. 16)}$$

with $f(\theta) = \sin^2\frac{\theta}{2}\cos\frac{\theta}{2}\sin 2\theta$ and $g_2(\theta,\Phi) = \frac{1}{1-\nu}\frac{g_1^2(\theta,\Phi)\sin\Phi\cos\theta}{\cos^3\frac{\theta}{2}}$

The scale of contributions of local mode II and mode III displacements to the closure level are given respectively by the functions f and g_2. The parametric angle variations of these functions are given in Fig. 5. This figure shows that mode II contribution are generally higher than mode III, however, particularly at low θ angles the mode III contribution to the overall crack closure level predicted by this model are of the same order of magnitude as mode II contribution and represent a significant percentage of the closure level at low θ angles.

2.4 Crack path dependency

In the above model, residual shear displacements giving rise to RICC are calculated on the basis of forward and reverse loads applied: as such the applied R-ratio appears in Eq. 16. Whilst cyclic loading at the first asperity encountered along a crack path may be expected to experience the applied R-ratio, the loading and unloading seen by the crack

tip at subsequent points will of course be attenuated if crack closure occurs, therefore an effective R-ratio may be considered as the crack progresses through several deflections. As such, an iterative model is produced, where a crack is propagated through several turning points sequentially, where the effective R-ratio at each successive point is based on the closure levels generated by the previous one. In practise it is seen that closure levels for propagation through multiple deflections become stable after 3 - 4 individual crack turning points.

Typical results for this 3-dimensional model are presented in Fig. 6. The respective contributions of mode II and mode III are again highlighted in this figure.

3. Experimental

3.1 Materials

Six Al-Cu-Mg-X alloys were rolled by QinetiQ plc, Farnborough UK, in the form of narrow plates of 150x20mm cross-section, compositions are shown in Table 1 and optical micrographs are shown in Fig. 7. In particular the alloys cover variations in Cu/Mg ratio, Li content and dispersoid type. Alloys A, B, D and E have similar Cu/Mg ratios whilst a higher and lower Cu/Mg ratios are evident in alloys C and F. Alloys A and B have the highest Li content. Alloys D, E and F contain intermediate amounts of Li whilst the Li content in alloy C is low. Dispersoids are Mn-containing in alloys B and C, Zr-containing in alloys A, E and F, whilst Alloy D contains both Zr- and Sc-containing dispersoids. The plates were supplied in a solutionised, quenched and stretched form. Extensive study of these alloys microstructure was performed using TEM and DSC and is presented in refs. [15,16,17,18]. For the present study, all alloys were artificially aged at 190ºC for 12

hours. Typical mid-thickness grain structures for the different alloys are shown in Fig. 1 and their respective grain sizes (mean intercepts in the T and S directions) are given in Table 2. Key features of the grain structures may be identified as follows: alloys B and C have relatively large, recrystallized grain structures, whilst alloys E and F are partially recrystallized with relatively large grains. Alloys A and D are partially recrystallized and exhibit a relatively fine grain structure and sub-structure. The Sc+Zr containing alloy D structure is seen to be particularly fine, with measured dimensions of the order of ~10μm in the T-direction. Key microstructural features of the alloys for the purpose of the present study are summarized in Table 3 [16]. The tensile properties for all alloys heat treated for 12 hours at 190°C are summarised in Table 4.

3.2 Fatigue testing

Conventional fatigue crack growth tests were performed in air at room temperature using an Instron 8501 servo-hydraulic machine. Compact-tension (CT) specimens were tested at a stress ratio (R) of 0.1 with a 20Hz frequency according to ASTM E647 [19]. The specimen thickness was 16mm and the gauge length 32mm. Conventional load shedding was used to obtain $da/dN \sim \Delta K$ curves. A direct current potential drop (DCPD) technique was used to monitor crack length. A crack mouth clip gauge was used to obtain conventional compliance curves. Measurements for closure determination were performed at a reduced load frequency of 1Hz. A non-subjective curve-fitting method was used to measure closure levels (a linear fit was made to the upper linear part of the compliance curve, whilst a quadratic function was fitted to the lower non-linear part), the details of which may be found elsewhere [20].

3D profiles of fracture surface roughness were obtained using a Rank-Hobson Talysurf stylus instrument [21]. Profiles were measured over a 2x2 mm area using 164 line scan corresponding to an in-plane measurement resolution of 12μm. Depth resolution is of the order of 0.1μm.

4. Results and Discussion

4.1 Fatigue tests results

Fig. 8 shows the da/dN vs. ΔK results for the 6 different alloys, whilst Table 3 provides a qualitative summary of the key microstructural features and crack growth resistance of the materials. In particular, the following points may be highlighted:

- Alloys A and B: the primary difference in alloy A compared to alloy B is the nature of dispersoids and, consequently the grain structure, with alloy B having large, recrystallized grains compared to the mostly unrecrystallized, fine grain structure in alloy A. As such, large, recrystallized grains are seen to enhance fatigue performance in alloy B compared to alloy A, in keeping with the results of Kirby et al. [22]. This is also highlighted by the relatively poor performance of alloy D, exhibiting a very fine structure.

- Alloys B and C: the primary difference between alloy B and C exists in the solute content (Cu + Mg content). As such, some detrimental effect of an increased content of non-shearable S/S′ precipitates content in alloy C is suggested. However, this effect in these alloys is convoluted to a difference in Li content. Though the effect of Li is not explicitly separated in these alloys, a beneficial effect of increased Li content may also be suggested here.

- Alloys E and F: the main difference between alloy E and alloy F is a higher Mg content in alloy F. Alloy E has better fatigue crack growth performance than alloy F as shown in Fig. 7**,** suggesting a detrimental influence of increased Mg.

Other influences have also been reported and may be present in those alloys such as highly textured grain structures in aluminium alloys, and particularly Al-Li alloys, which are beneficial to the alloy fatigue life due to the low degree of misorientation between grain boundaries limiting their effectiveness as barriers to dislocation motion and, hence, favouring inhomogeneous fatigue deformation and hence crack growth along slip bands [23].

To summarize, within the group of alloys assessed, there is clear evidence of microstructural influence on crack growth behaviour. The relative effect of crack closure on the fatigue performance of the different alloys is illustrated in Fig. 9. Fig. 8 and Fig. 9 show that the closure levels of the different alloys scale reasonably well with their fatigue performance. Alloy D has the lowest closure levels and is associated with the worst fatigue performance. Closure levels for alloy A and C are above alloy D and below alloys B, E and F and similarly exhibit intermediate fatigue crack growth rates. The alloys exhibiting the highest closure levels (alloys B, E and F), have the best fatigue crack growth performance.

4.2 Modelling results

Typical results from the Talysurf surface mapping are shown in Fig. 10 with corresponding surface fractography for alloys A, B and D. This study considers the low ΔK region for all these alloys where RICC is thought to be most influential. This figure

clearly shows that the crystallographic features of fatigue crack growth at low ΔK in alloy B are related to a rough surface topology. Alloy C, E and F exhibit similar features. The more ductile character of alloy A and D fracture surfaces is reflected by smoother surface map.

In order to apply the model above to experimental behaviour, geometrical parameters need to be identified from the real fatigue fracture surfaces: the deflection length L and the deflection angles θ and Φ are required. Fig. 11 details the parameters extraction from the fracture surface profile. θ_i angles are defined as the angles just before a turning point in a given crack profile (Fig. 11c) as it is the local mixity of loading immediately prior to a turning point that is considered critical in the present modelling approach. L_i distances are then defined as the distance along the horizontal axis between two consecutive turning points (Fig. 11c). Φ_i are the angles associated with θ_i in the direction perpendicular to the crack propagation direction (Fig. 11d). As a given crack will contain many asperity points, a high number of (θ_i,Φ_i,L_i) triplet parameters is obtained for any one fracture surface analysed. Physical observation of crack closure phenomenon [8] using tomography techniques indicated that closure only occurs at relatively small number of 'high points' within a given crack wake. Therefore to correctly represent the fatigue fracture surface with a set of (θ_i,Φ_i,L_i) average parameters, only geometrical parameters associated with the maximum crack closure point for each line representing the advancing crack front was considered. Such distributions of (θ_i,Φ_i,L_i) parameters for alloy A is shown in Fig. 12. Subsequently the average of these parameters is taken as the θ, Φ and L giving a general indication of roughness and RICC across the whole fracture surface. It should be noted that considering only parameters giving maximum crack

closure puts more emphasis towards crack deflections extending over several grains which may be expected to give higher crack closure (rougher macroscopic fracture surface). As such, the spatial resolution limitation of the Talysurf measurements (12μm), which for alloy A and D is comparable to their grain size, still enables to detect these deflections extending over several grains and thus does not adversely affect deflection length measurements for use in the crack closure model described above. However, it is acknowledged that fine scale crack path data is lacking from these measurements for a more complete qualitative discussion of the crack interaction with single grains. Furthermore, although these parameters are not an exact representation of the fatigue fracture surface, it is proposed that in first approximation the systematic estimation of these parameters is able to show a proportional relationship between the fatigue fracture surface roughness and those parameters. The parameters extracted from the surface mapping are given in Table 5. It can be seen that alloys having a rough fracture surface, such as alloys B and E, have longer deflection lengths L and also higher twist deflection angle Φ. Conversely, alloy D, which exhibits a relatively flat fracture surface has the lowest deflection angles and deflection length. As such, the observed roughness of the fatigue surfaces seems to scale reasonably well with these extracted parameters. Only the deflection angles θ of the rougher alloys E and B do not seem to scale compared to alloys from the medium range A, C and F.

Fig. 13 shows the relationship between deflection length and grain size in the T direction for the various materials. No clear trend can be observed in Fig. 13: this is not unexpected as complex relationships between the deflection lengths and the texture and/or the slip planarity of the materials are known to occur [23].

Fig. 14 shows Alloy D and F parameters applied to the analytical RICC models (Eq. 7 and Eq. 16). All the alloys exhibit the same cyclic behaviour. For Eq. 16, the values of λ and β were chosen to give the best fit with experimental data and were respectively: 0.4 and 3.3. Considering the crack closure behaviour predicted by Eq. 16 illustrated in Fig. 14, it can be seen that after two iteration of the model, which is equivalent to the crack going through two successive deflections, the maximum closure level is stable, i.e. considering an effective R ratio in the model will give an increase of the closure level over the first deflection but will stabilize thereafter. Eq. 16 clearly predicts higher closure values compared to Eq. 7.

The comparison between measured experimental crack closure stress intensity factors $K_{cl\text{-experimental}}$, which is taken as the average K_{cl} over the surface where the Talysurf mappings were performed, and the analytical predictions from Eq. 16 of the crack closure stress intensity factor, $K_{cl\text{-predicted}}$, is shown in Fig. 14 with β=3.3. It may be seen that the model predicts the general trend of K_{cl} for all these alloys. A distinct linear trend in the data is shown in Fig. 15. Overall it may be seen that for the present relatively wide range of microstructures and corresponding crack growth behaviours, the current closure model approaches (both 2D and 3D versions) provide a reasonable description of how fracture surface features may influence closure contributions to crack growth resistance. It can be seen in Fig. 15 that although the 2D model predicted K_{cl} values exhibit a general correlation, they substantially underpredict the experimentally measured K_{cl} for low and intermediate values (2-5MPa$\sqrt{}$m). As such, the 2D model can be expected to give reasonable trend approximation of crack closure behaviour whilst the 3D model appears to be more quantitatively accurate especially for intermediate experimental K_{cl} values

(3.5-5MPa√m). Furthermore, Fig. 16 shows the respective contribution of mode II and mode III deformation to the closure level of all the alloys and illustrates the relative importance of mode III deformation. In the alloys with the lowest stress intensity factor at closure, A, B, C, D and E, mode III deformation represents more than 30% and up to 60% of the total closure level. On the opposite in the alloy with the highest $K_{cl\text{-experimental}}$, F, mode III deformations accounts only for ~20% of the total closure. This tends to indicate that high closure values are associated with high tilting angles rather than twisting angles. Also it further emphasises the importance of considering three dimensional effects, especially at low deflection angles, in relation to crack closure in aluminium alloys.

The relative contribution of RICC to the overall closure behaviour when considering the predictions shown in Fig. 15 may also be significant. Even in the near-threshold regime PICC may be expected to have a significant influence. It has been shown that when crack asperity size, L, are small relative to the plastic zone size, r_p, RICC effects are predicted to decrease significantly [9] and closure may be expected to be generated via PICC mechanism. As a corollary, when crack asperity sizes are large relative to the plastic zone size, shear displacements are expected to be more effective in generating closure. L/r_p values are given in Table 5 for all alloys. Whilst alloy C which possesses the highest L/r_p ratio exhibits the best K_{cl} prediction, alloy A with a low L/r_p ratio also shows reasonable prediction and alloy D with a high L/r_p ratio has relatively poor model prediction. The quantification of the relative contribution of PICC and RICC to crack closure in the near-threshold regime is therefore not straightforward and would require further investigation.

5. Conclusions

An existing analytical model of RICC has been extended to include the contribution of mode III twist deformation to closure levels. The respective contribution of mode II and mode III displacement to the total closure level has been analysed, confirming the predominance of mode II deformations influence on crack closure at high tilting angles but also the significant contribution of mode III deformations particularly for low to intermediate tilting angles. Fatigue crack growth tests were performed on various 2xxx aluminium alloys exhibiting a range of microstructural features, giving rise to a range of crack growth modes and corresponding crack growth resistance characteristics. A relatively straightforward method to extract geometrical parameters from fatigue fracture surfaces was proposed. Though it is acknowledge that the parameters obtained are not exact representations of crack deflection angles and lengths, they are nevertheless a measure of fracture surface roughness levels directly related to the micromechanical origins of the present RICC modelling framework. Comparison between the results given by analytical modelling and experimentally measured values of crack closure are satisfactory considering the errors arising from both the experimental measurements methods and the approximations performed using the analytical model, with basic trends in increasing and decreasing closure levels for different alloys being well represented.

Acknowledgement

The technical and financial support of the EPSRC, Airbus and QinetiQ plc are gratefully acknowledged.

References

[1] J.C. Newman, W. Elber, Mechanics of Fatigue Crack Closure, Special Technical Publication 982, American Society for Testing and Materials, Philadelphia, 1988.

[2] R.C. McClung, J.C. Newman, Advances in fatigue crack closure measurement and analysis, Special Technical Publication 1343, American Society for Testing and Materials, 1998.

[3] Suresh S, Vasudevan AK, Bretz PE. Mechanisms of slow fatigue crack-growth in high-strength aluminum alloys - role of microstructure and environment Metall Trans A 1984;15:369-379.

[4] Carter RD, Lee EW, Starke EA, Beevers CJ. The effect of microstructure and environment on fatigue crack closure of 7475-aluminium alloy. Metall Trans A 1984;15A:555-563.

[5] Suresh S, Ritchie RO. A geometric model for fatigue crack closure induced by fracture surface-roughness. Metall Trans A 1982;13A:1627-1631.

[6] Llorca J. Roughness-induced fatigue crack closure-A numerical study. Fatigue Fract Eng Mater Struct 1992;15:655-669.

[7] Guvenilir A, Stock SR. High resolution computed tomography and implications for fatigue crack closure modelling. Fatigue Fract Eng Mater Struct 1998;21:439-450.

[8] Toda H, Sinclair I, Buffiere JY, Maire E, Connolley T, Joyce M, Khor KH, Gregson PJ. Assessment of the fatigue crack closure phenomenon in damage-tolerant aluminium alloy by in-situ high-resolution synchrotron X-ray microtomography. Phil Mag 2003;83:2429-2448.

[9] Kamp N, Parry MR, Singh KD, Sinclair I. Analytical and finite element modelling of roughness induced crack closure. Acta Mater 2003;52:343-353.

[10] Rice JR, Fatigue Crack Propagation. ASTM STP 415. Philadelphia: American Society for Testing and Materials, 1967. p 247.

[11] Li C, Acta Metall Mater 1990;38:2129

[12] Ewalds HL, Wanhill RJH, Fracture mechanics. Edward Arnold, editor. London, 1984.

[13] Parry MR, Phd Thesis, University of Southampton, 2001.

[14] Faber KT, Evans AG. Crack deflection processes-1. Theory. Acta Metall 1983;31:565-576.

[15] Starink MJ, Sinclair I, Gao N, Kamp N, Gregson PJ, Pitcher PD, Levers A, Gardiner S. Development of new damage tolerant alloys for age-forming. Mater Sci Forum 2002:396-402;601-606.

[16] Gao N, Davin L, Wang S, Cerezo A, Starink MJ. Precipitation in stretched Al-Cu-Mg alloys with reduced alloying content studied by DSC, TEM and atom probe. Mater Sci Forum 2002;396-402:923-928.

[17] Gao N, Starink MJ, Davin L, Cerezo A, Wang S, Gregson PJ. Microstructure and precipitation in Al-Li-Cu-Mg-(Mn,Zr) alloys. Mater Sci Tech 2005:21;1010-1018.

[18] Davin L, Cerezo A, Gao N, Starink MJ. Characterisation of the precipitation in Al-Li-Cu-Mg-(Mn, Zr) alloys. Surf Interface Analysis 2004:36;589-593.

[19] ASTM standard E 647, Annual book of ASTM Standards, American Society for Testing and Materials, Philadelphia, PA, 1996, p. 570.

[20] Xu Y, Gregson PJ, Sinclair I. Systematic assessment and validation of compliance-based crack closure measurements in fatigue. Mater Sci Eng A 284 2000;284:114-125.

[21] Stout KJ, Sullivan PJ, Dong WP, Mainsah E, Luo N, Mathia T, Zahouani H, The development of methods for the characterisation roughness in three dimensions, Commission of the European Communities, Directorate General XII, Science, Research and Development, Report EUR 15178 EN, 1993.

[22] Kirby BR, Beevers CJ. Slow fatigue crack growth and threshold behavior in air and vacuum of commercial aluminum alloys. Fatigue Eng Mater Struct 1979;1:203.

[23] Rao KTV, Ritchie RO. Fatigue of Aluminum-Lithium Alloys. Int Mater Rev 1992;37:153-183.

Alloy	Cu	Mg	Li	Zr	Mn	Sc
A	2.27	1.03	1.56	0.106	-	-
B	2.24	0.94	1.60	-	0.42	-
C	4.30	1.46	0.17	0.06	0.43	-
D	2.08	0.97	0.55	0.11	-	0.21
E	2.22	0.9	0.57	0.11	-	-
F	1.48	1.43	0.54	0.11	-	-

Table 1. Alloy compositions (weight %).

Alloys		A	B	C	D	E	F
Grain size* (µm)	S	11	64	59	5	59	36
	T	18	83	142	9	74	60

* line intercept measurements

Table 2. Grain sizes measured for alloys A-F.

Increasing crack growth rate ↓

Alloys	Grain Structure	Solute elements	Precipitates	Dispersoids
Alloy B	Coarse Recrystallised	High Li	Some δ′ + S phase	Al_7Cu_2Mn
Alloy E	Coarse part. Rex*	Mid Li	S phase	Al_3Zr
Alloy A	Fine Unrecrystallised	High Li	Some δ′ + S phase	Al_3Zr
Alloy F	Coarse part. Rex*	Mid Li, excess Mg	S phase	Al_3Zr
Alloy C	Coarse Recrystallised	Low Li	S phase	Al_7Cu_2Mn
Alloy D	Very fine	Mid Li	S phase	$Al_3(Zr,Sc)$

* Partially recrystallised alloys

Table 3. Summary of alloy properties. Alloys are ordered according to their general fatigue performance.

Alloys	**A**	**B**	**C**	**D**	**E**	**F**
Tensile strength (MPa)	399	393	493	397	364	323
Yield strength (MPa)	365	343	464	369	335	273
Elongation (%)	14	13	10	15	16	17

Table 4. Tensile properties.

Alloys	A	B	C	D	E	F
θ	23	24	25	18	21	30
Φ	32	34	32	21	38	28
L (μm)	35	59	49	35	88	58
L/r_p^*	0.93	1.25	4.02	2.75	1.96	0.70

$^* r_p \sim \left(K_{\mathrm{Im}ax}/\sigma_{ys}\right)^2$

Table 5. Geometrical parameters associated with alloy fracture surfaces.

List of Figure captions:

Fig. 1. (a) Definitions of crack deflection angle θ, and deflection length. (b) Geometry of the 2D crack deflection model [9].

Fig. 2. Analytical RICC model predictions (Eq. 7)

Fig. 3. Definitions of crack deflection angle Φ and local stress intensity factor k_3.

Fig. 4. Schematic illustration of the effect of mode II and mode III deformations on the formation of asperities projected along (a) the (yz) and (b) the (xz) axes.

Fig. 5. Parametric variation of the functions (a) f, (b) g_2 and (c) $f+g_2$.

Fig. 6. Analytical RICC model prediction (Eq. 16).

Fig. 7. Optical micrographs of polished and etched sections of alloys A (typical grain structure for Zr-containing alloys), B (typical of Mn-containing alloys) and D (Zr+Sc-containing alloy).

Fig. 8. Fatigue crack growth rate vs. ΔK for alloys A - F for R=0.1.

Fig. 9. Closure results from crack mouth clip gauge data for alloys A-F.

Fig. 10. SEM fractography and Talysurf fracture surface mapping for a) alloy A: fine grains-partially recrystallized, b) alloy B: coarse grains-recrystallized and c) alloy D: very fine grains partially recrystallized.

Fig. 11. Extraction of deflection length and angles from fatigue fracture surface profile a) Talysurf fatigue fracture surface profile for alloy A, b) Wireframe representation of top left corner from a), c) individual (xy) line profile and related parameters θ_i and L_i, and d) individual (xy) line profile associated with θ_4 and related parameter Φ_4.

Fig. 12. Distribution of θ_i, Φ_i and L_i for Alloy A.

Fig. 13. Grain size (T direction) vs. L values obtained from Talysurf profiles.

Fig. 14. Analytical model predictions for Eq. 7 and Eq. 16 applied to Talysurf parameters determined for alloys D and F.

Fig. 15. Comparison between K_{cl} values measured experimentally and K_{cl} values predicted by the analytical model including mode III effects and effective R ratio (Eq. 15) with β=3.3.

Fig. 16. Percentage contribution of mode II and mode III deformation to the total closure level.

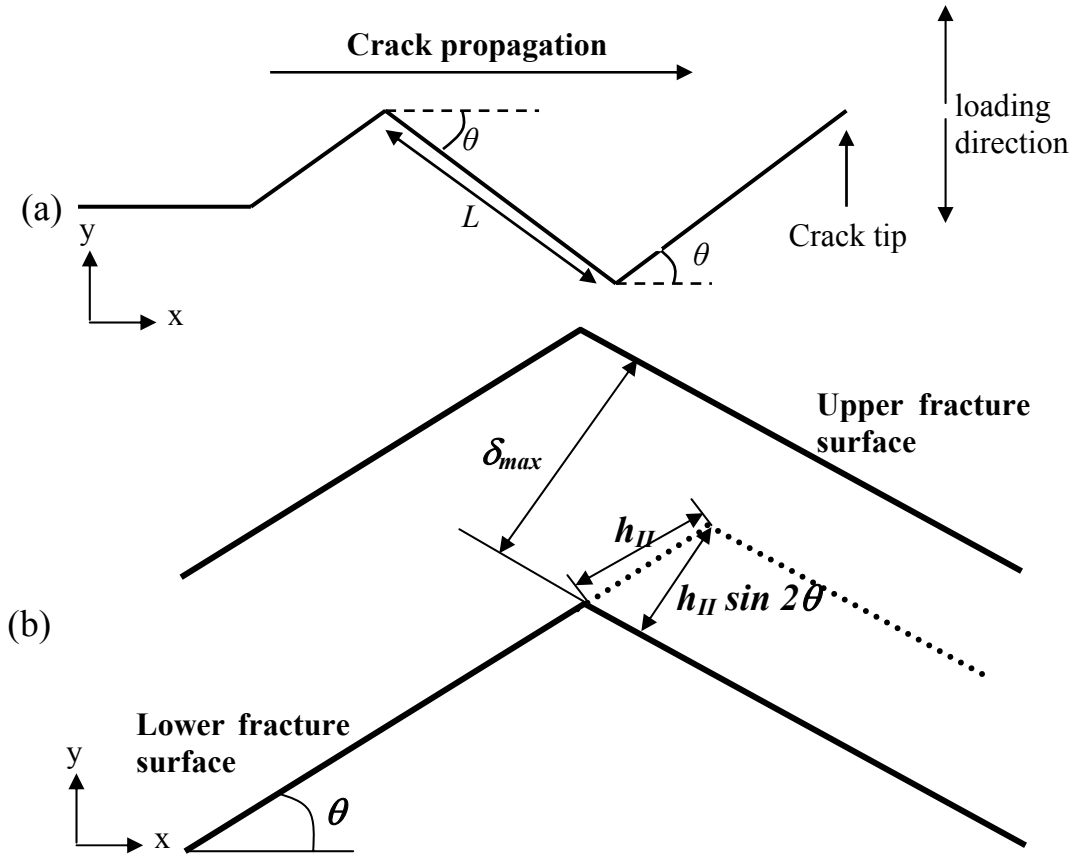

Fig. 1. (a) Definitions of crack deflection angle θ, and deflection length. (b) Geometry of the 2D crack deflection model [9].

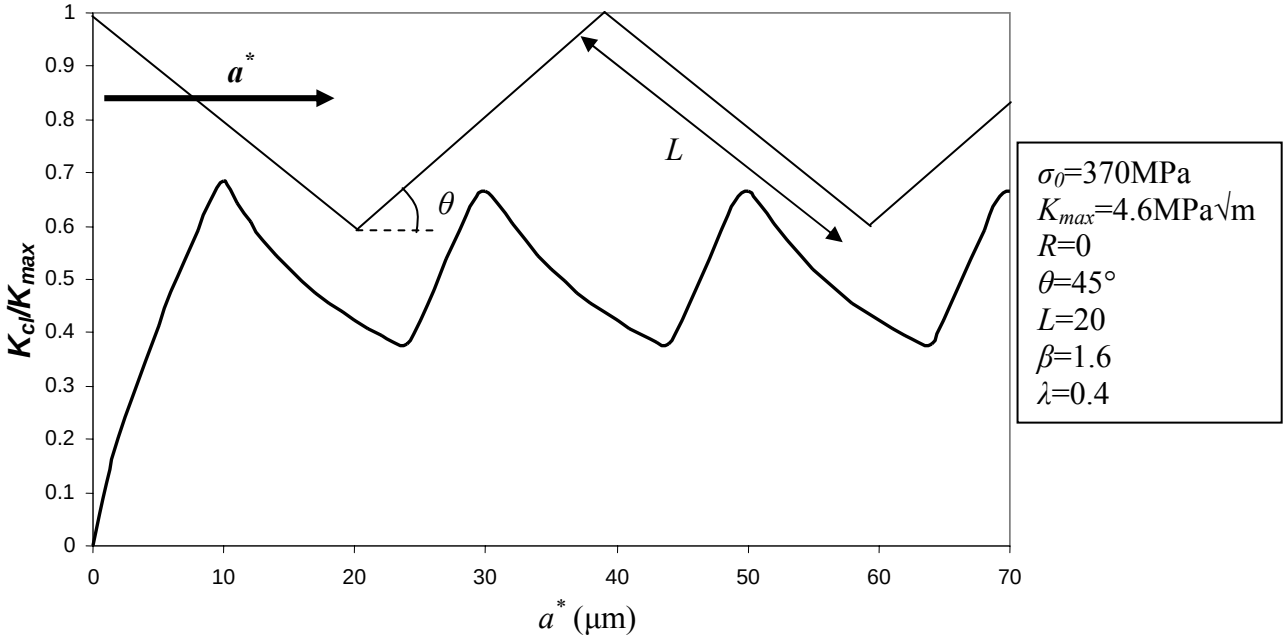

Fig. 2. Analytical RICC model predictions (Eq. 7)

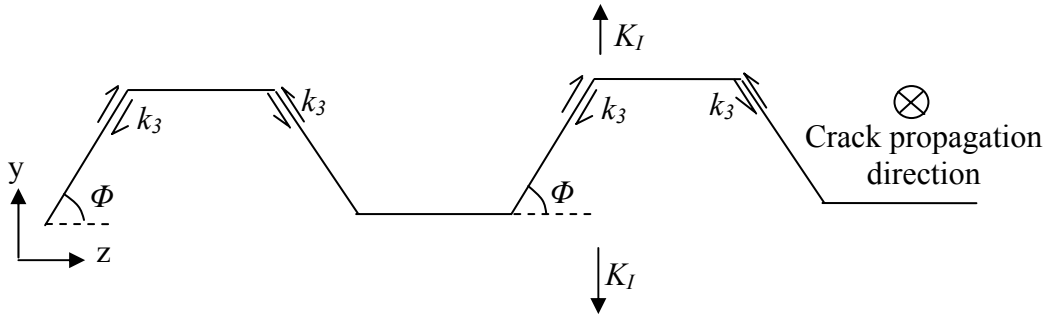

Fig. 3. Definitions of crack deflection angle Φ and local stress intensity factor k_3.

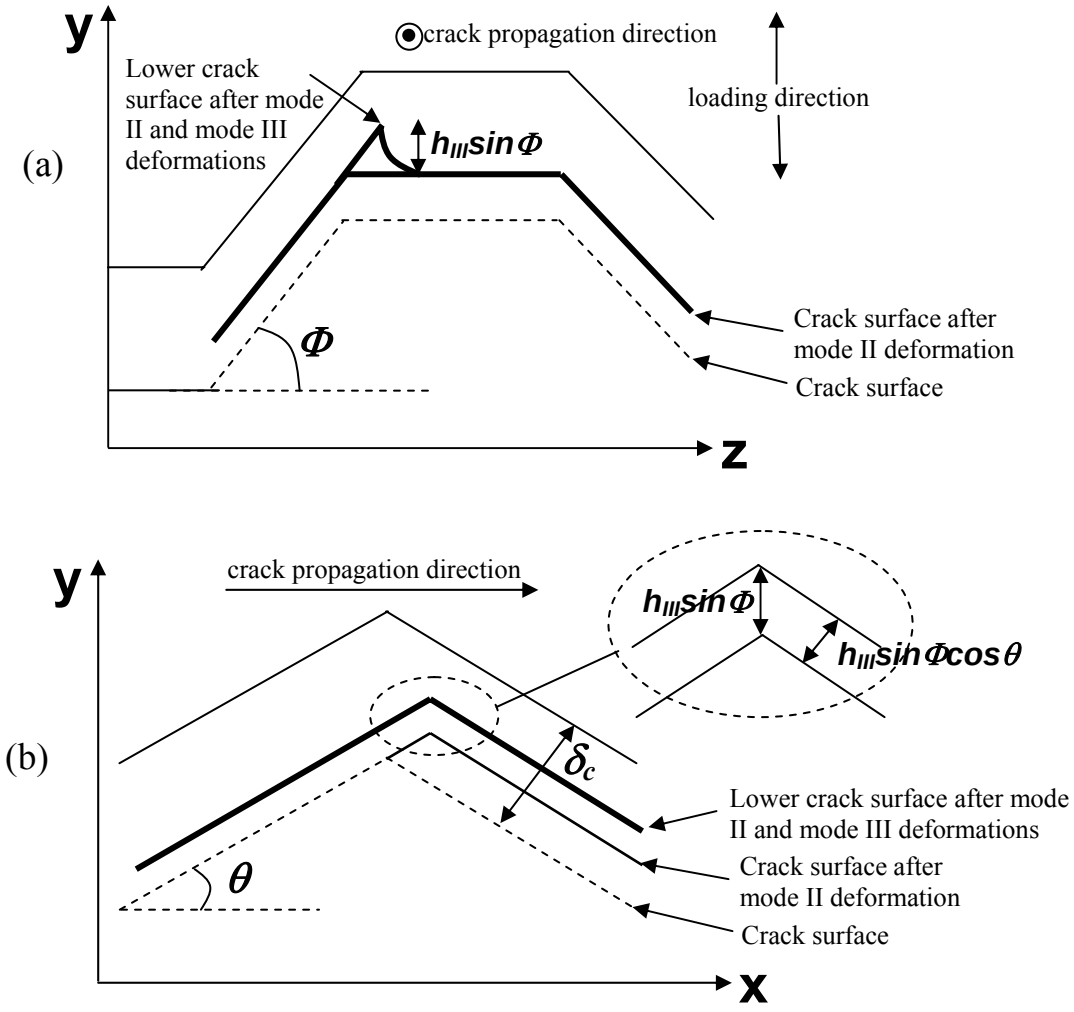

Fig. 4. Schematic illustration of the effect of mode II and mode III deformations on the formation of asperities projected along (a) the (yz) and (b) the (yz) axes.

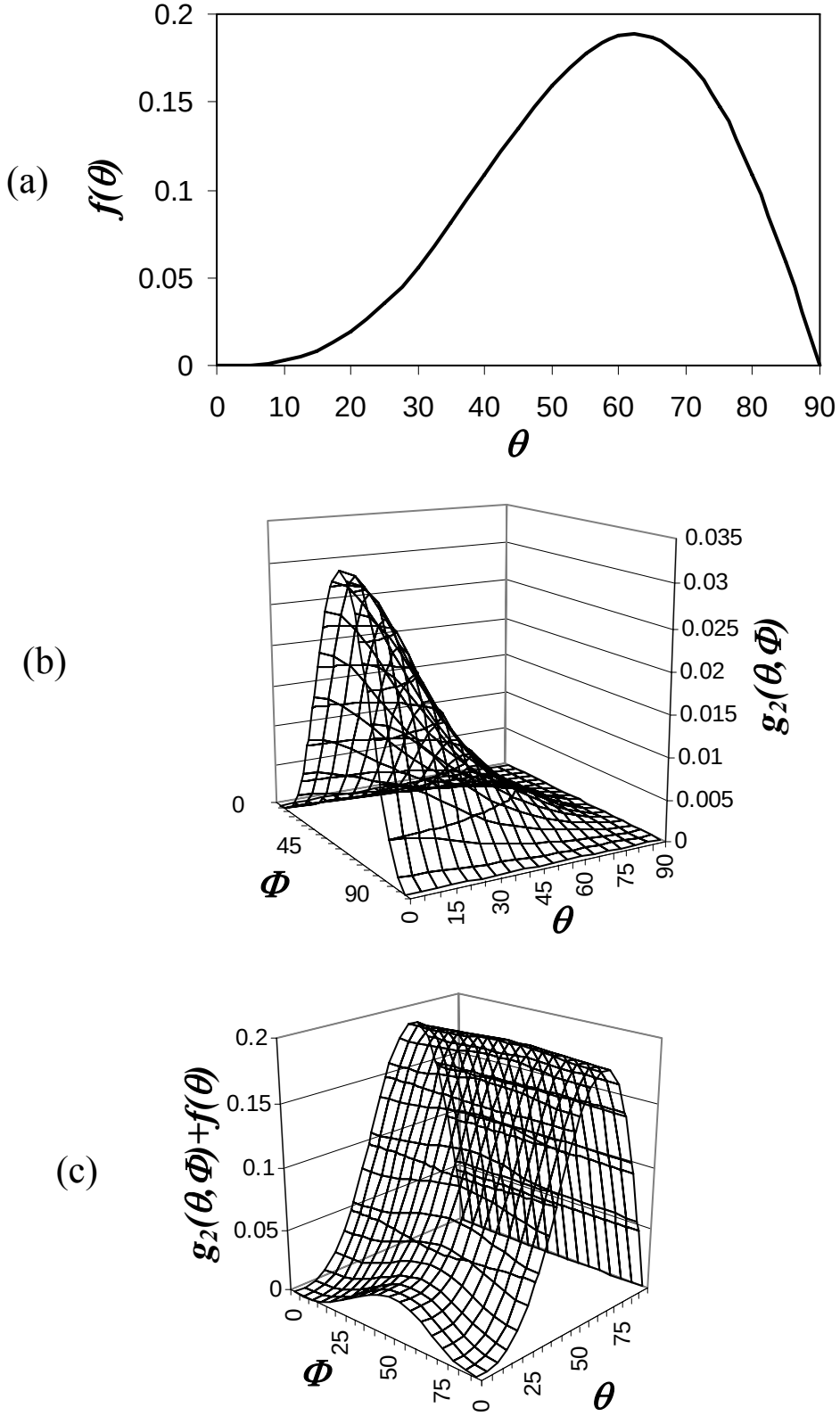

Fig. 5. Parametric variation of the functions (a) f , (b) g_2 and (c) f+g_2.

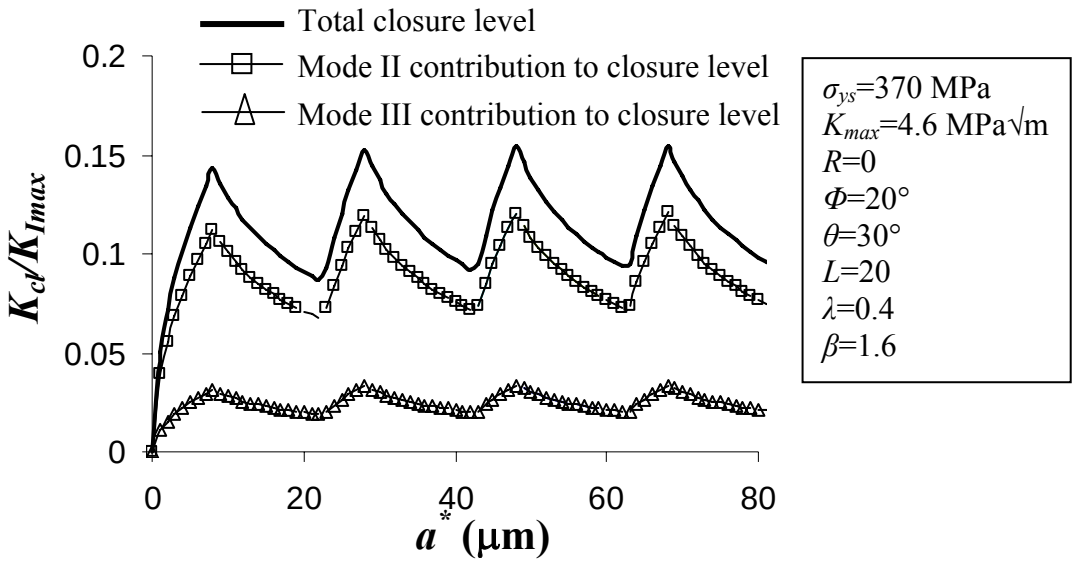

Fig. 6. Analytical RICC model prediction (Eq. 16).

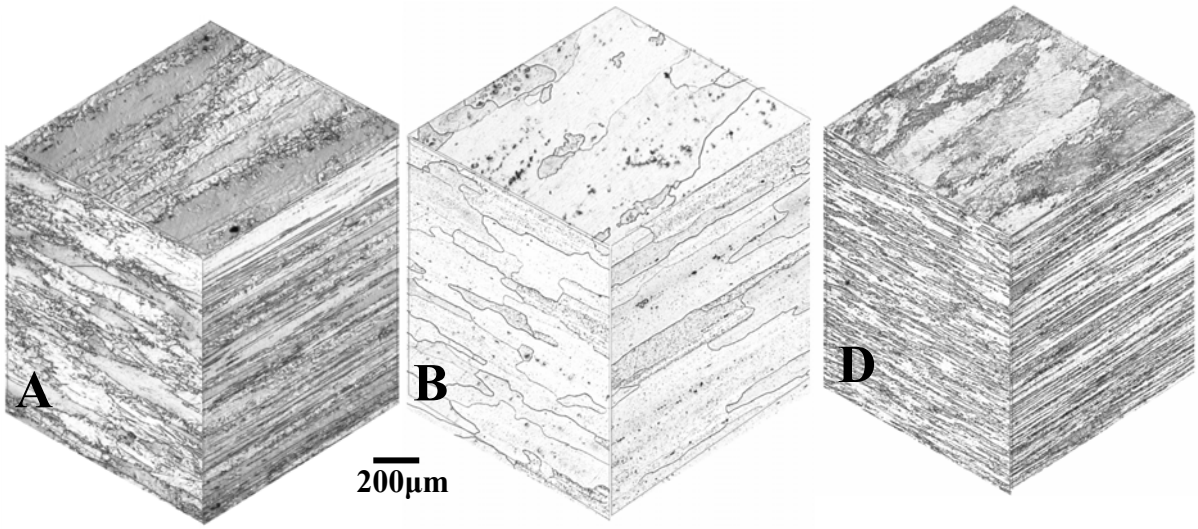

Fig. 7. Optical micrographs of polished and etched sections of alloys A (typical grain structure for Zr-containing alloys), B (typical of Mn-containing alloys) and D (Zr+Sc-containing alloy).

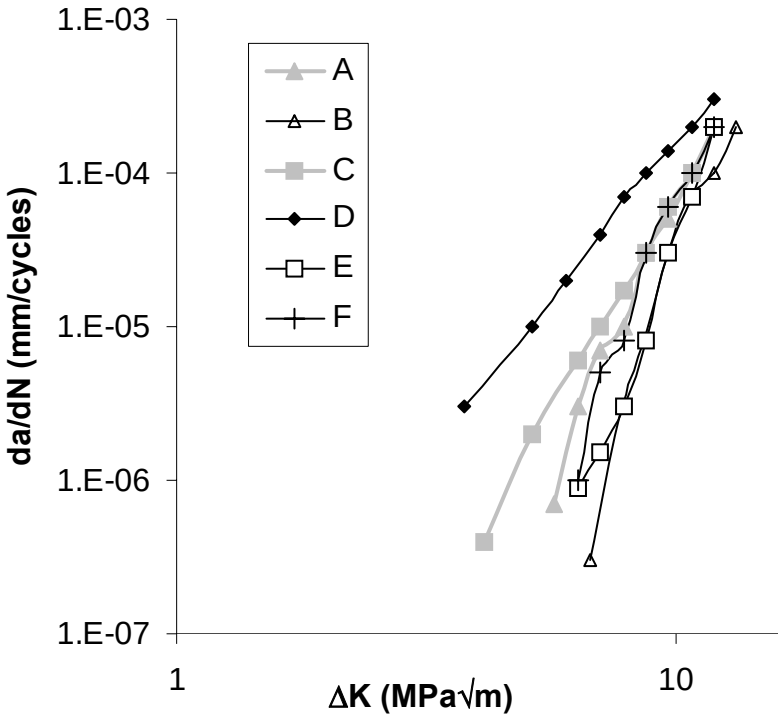

Fig. 8. Fatigue crack growth rate vs. Δ*K* for alloys A - F for *R*=0.1.

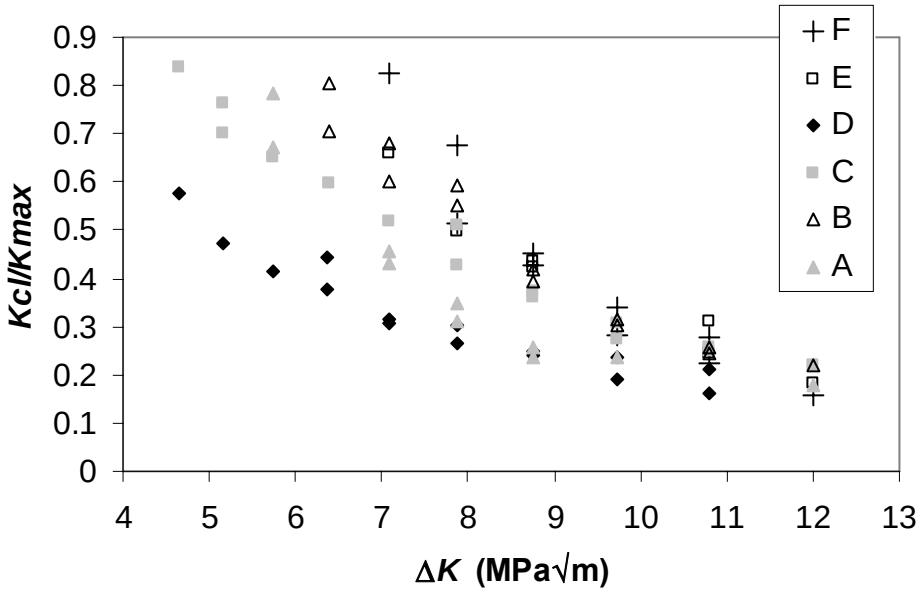

Fig. 9. Closure results from crack mouth clip gauge data for alloys A-F.

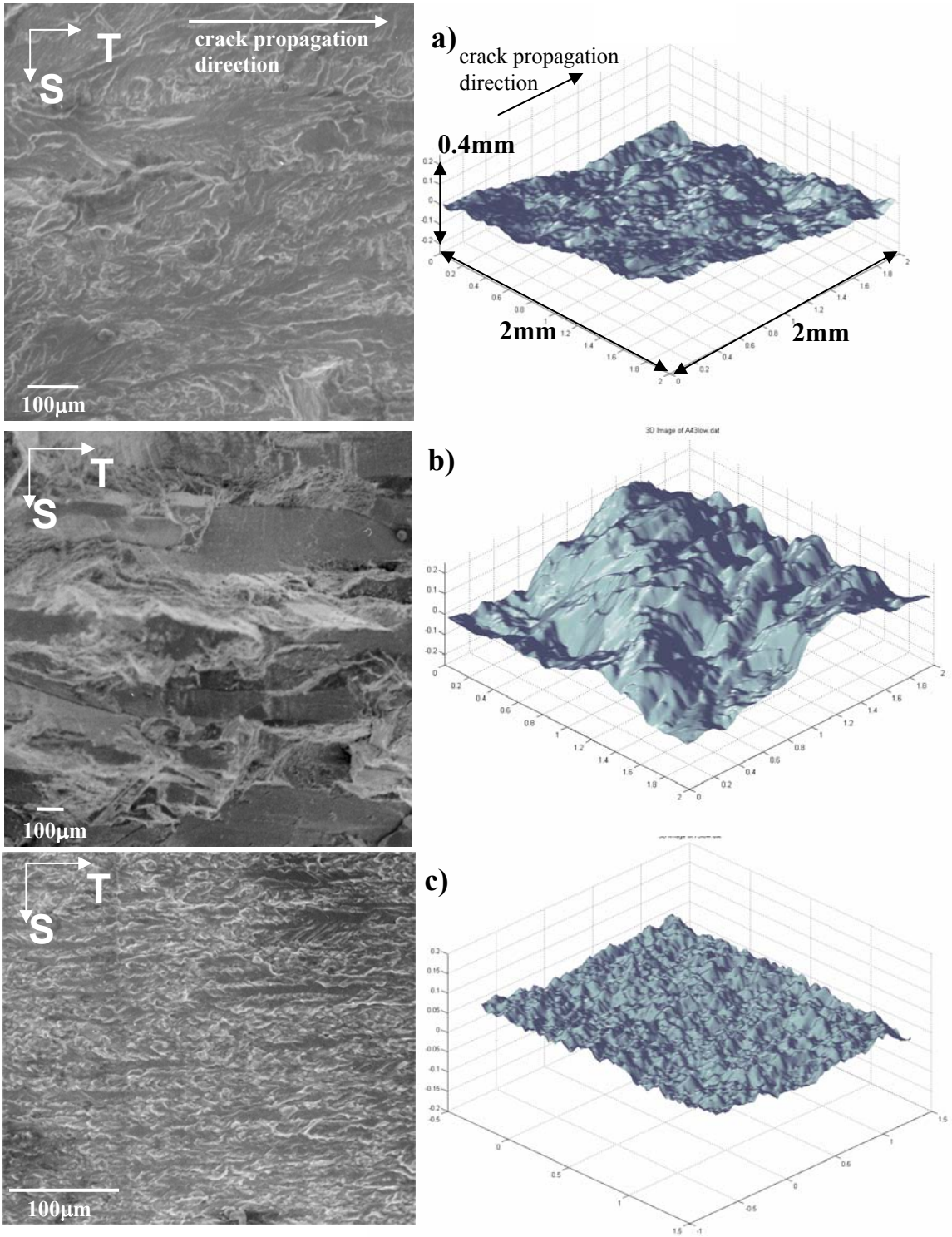

Fig. 10. SEM fractography and Talysurf fracture surface mapping for a) alloy A: fine grains-partially recrystallized, b) alloy B: coarse grains-recrystallized and c) alloy D: very fine grains partially recrystallized.

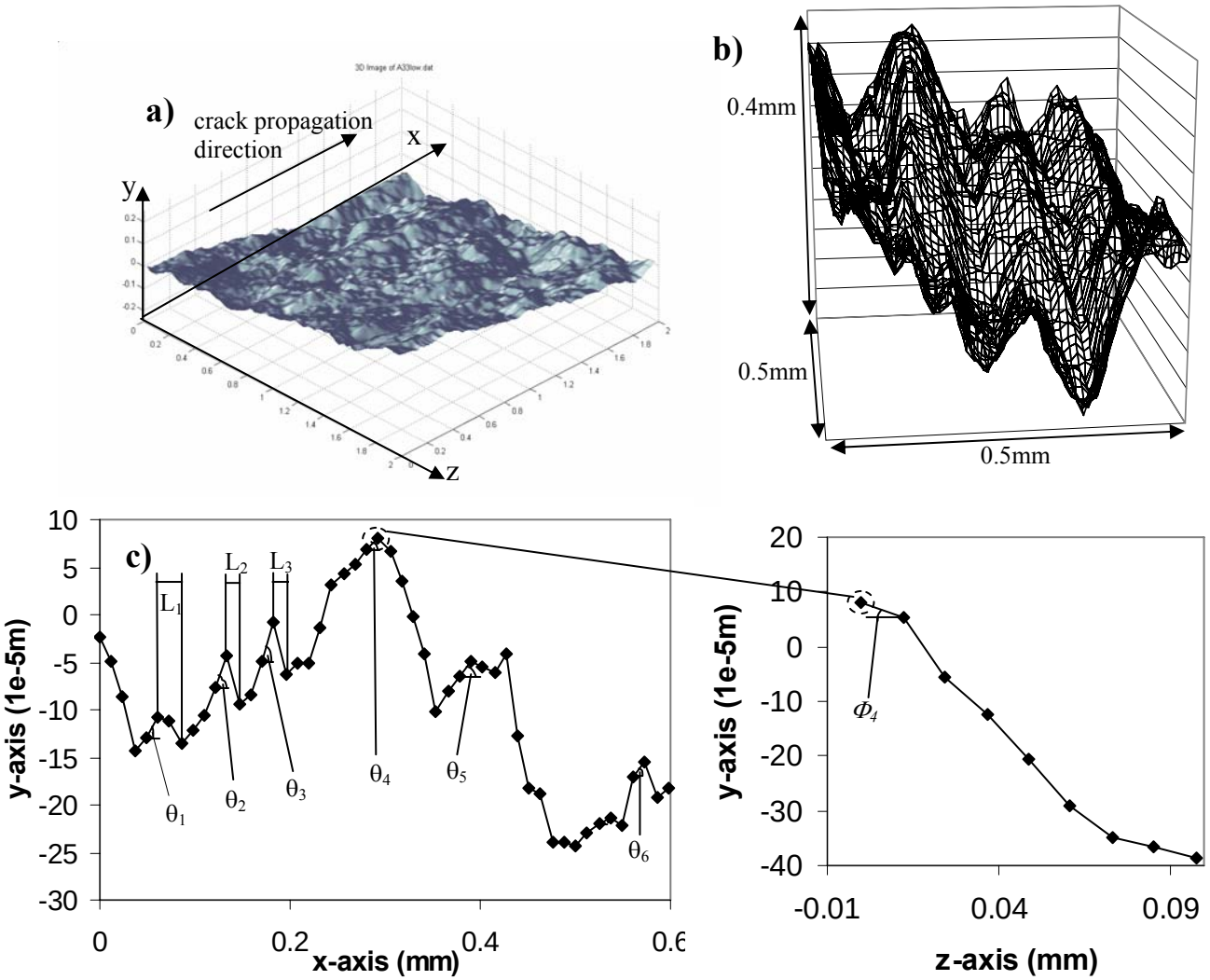

Fig. 11. Extraction of deflection length and angles from fatigue fracture surface profile a) Talysurf fatigue fracture surface profile for alloy A, b) Wireframe representation of top left corner from a), c) individual (xy) line profile and related parameters θ_i and L_i, and d) individual (yz) line profile associated with θ_4 and related parameter Φ_4.

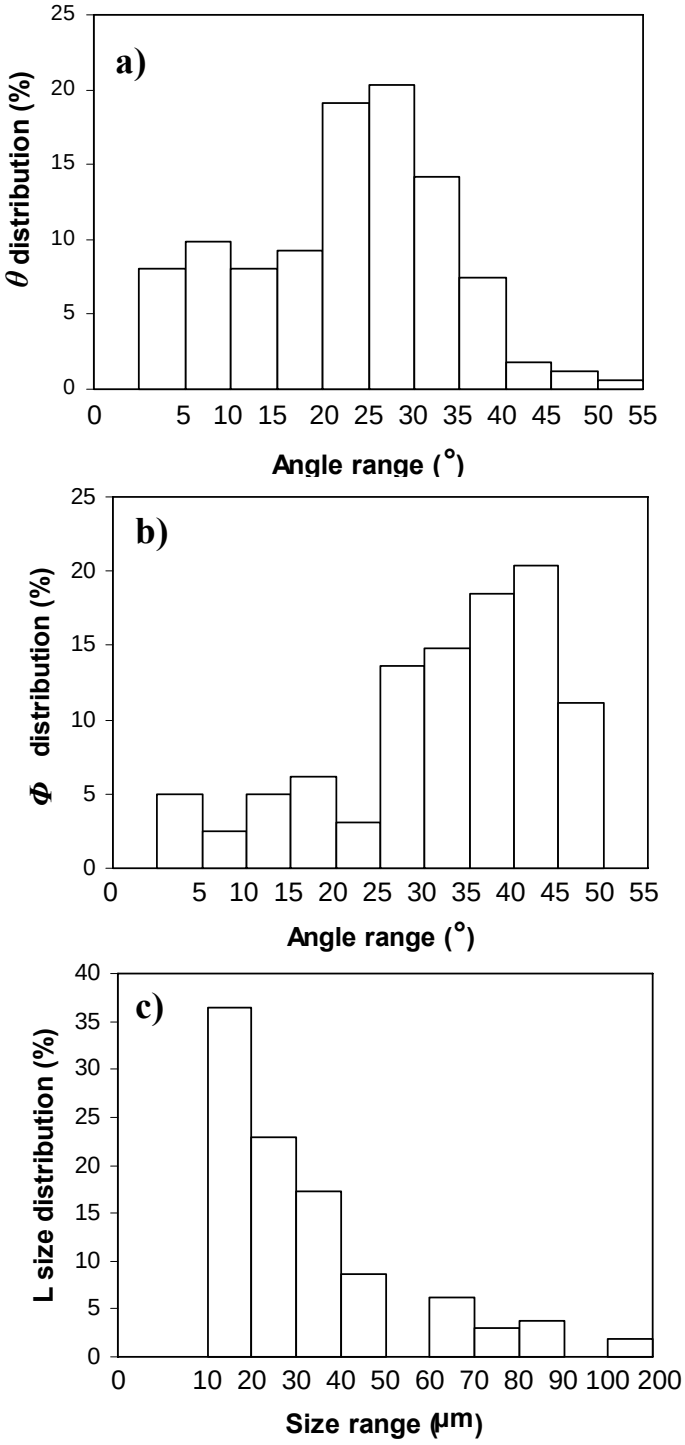

Fig. 12. Distribution of θ_i, Φ_i and L_i for Alloy A.

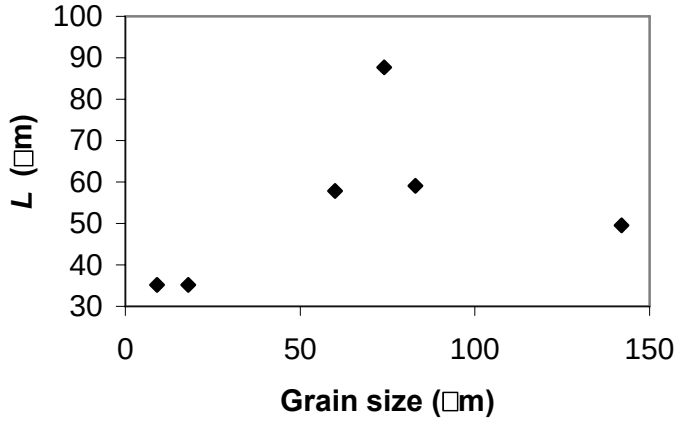

Fig. 13. Grain size (T direction) vs. *L* values obtained from Talysurf profiles.

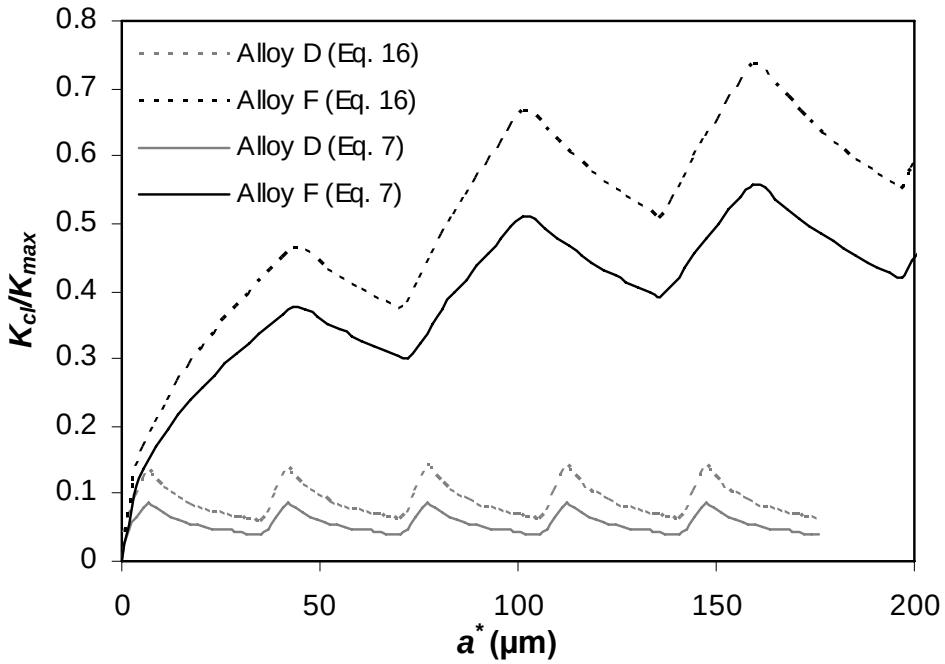

Fig. 14. Analytical model predictions for Eq. 7 and Eq. 16 applied to Talysurf parameters determined for alloys D and F.

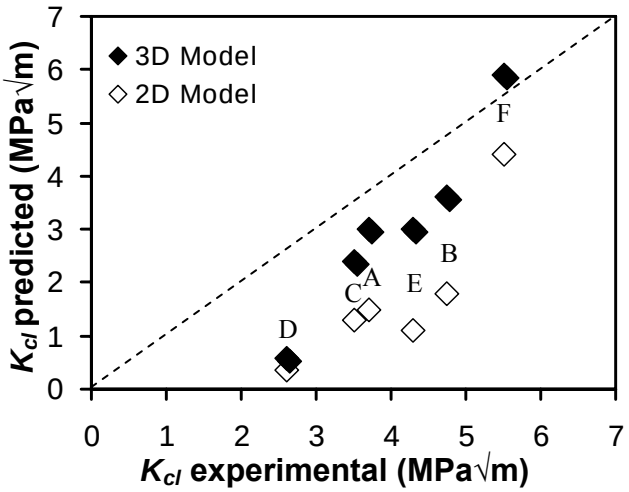

Fig. 15. Comparison between K_{cl} values measured experimentally and K_{cl} values predicted by the analytical model including mode III effects and effective R ratio (Eq. 16) with β=3.3.

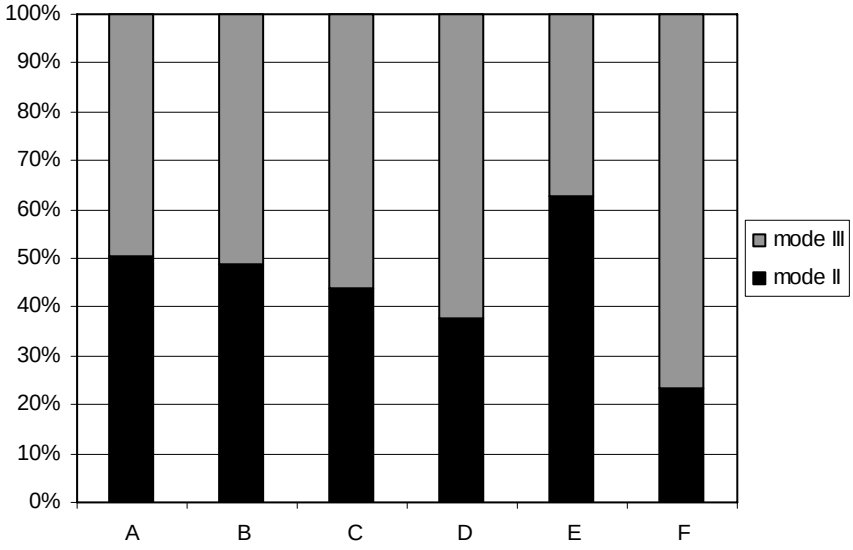

Fig. 16. Percentage contribution of mode II and mode III deformation to the total closure level.